Multistability in a family of DT–TTF organic radical based compounds $(DT–TTF)_4[M(L)_2]_3$ (M = Au, Cu; L = pds, pdt, bdt)†

João C. Dias,[a] Xavi Ribas,[b] Jorge Morgado,[ac] João Seiça,[a] Elsa B. Lopes,[a] Isabel C. Santos,[a] Rui T. Henriques,[ac] Manuel Almeida,*[a] Klaus Wurst,[d] Pascale Foury-Leylekian,[e] Enric Canadell,[b] José Vidal-Gancedo,[b] Jaume Veciana[b] and Concepció Rovira*[b]

Received 25th April 2005, Accepted 3rd June 2005
First published as an Advance Article on the web 27th June 2005
DOI: 10.1039/b505724h

The preparation of new charge transfer salts based on the DT–TTF donor and monoanionic square planar transition metal bisdichalcogenide complexes $M(L)_2$ (M = Au, Cu; L = pds, pdt, bdt, where pds = pyrazine-1,2-diselenolate, pdt = pyrazine-1,2-dithiolate, bdt = benzene-1,2-dithiolate) are reported and these salts are characterized by X-ray diffraction, EPR spectroscopy, electrical conductivity, thermoelectric power and static magnetization measurements, as well as tight-binding band structure calculations. Three compounds, $(DT–TTF)_4[Au^{III}(bdt)_2]_3$, $(DT–TTF)_4[Cu^{III}(pds)_2]_3$, $(DT–TTF)_4[Cu^{III}(pdt)_2]_3$, are members of a general family of compounds of DT–TTF with stoichiometry 4 : 3 as the previously reported $(DT–TTF)_4[Au^{III}(pds)_2]_3$. Although not strictly isostructural, all members of this family present a similar crystal packing motif of the donor and acceptor units and present a common pattern of first- and second-order phase transitions as seen in electrical transport and magnetic properties. The second-order phase transition is ascribed to a variation from dynamic to static charge ordering. With $[Cu^{III}(pdt)_2]$ and DT–TTF a 1 : 1 salt with formula $(DT–TTF)[Cu^{III}(pdt)_2]$ was also obtained. The structural differences and similarities between the four compounds $(DT–TTF)_4[M(L)_2]_3$ (M = Au, Cu; L = pds, pdt, bdt), that are related to their physical properties, and the reversible phase transitions observed are discussed.

Introduction

The investigation of compounds showing a magnetic spin-ladder behavior has attracted large interest among the physics and materials chemistry communities during the last few years.[1] The combination of the DT–TTF (dithiophene–tetrathiafulvalene) donor with different transition metal bisdithiolene monoanionic complexes ($[M(mnt)_2]^-$ (M = Au, Cu, Ni, Pt) and $[Au(i\text{-}mnt)_2]^-$), led to the discovery of a very interesting family of radical ion salts in which magnetic spin-ladder behavior was achieved when the anions are diamagnetic (M = Au, Cu).[2] A related and very attractive system based on the DT–TTF donor and the monoanionic $[Au(pds)_2]^-$ complex which presents a new structure type with a rare 4 : 3 donor : acceptor stoichiometry, $(DT–TTF)_4[Au(pds)_2]_3$, was recently reported.[3,4] This compound presents two transitions clearly seen in the electrical conductivity measurements, the first at 238 K and the second with a large hysteretic loop at 200–120 K.

Organic radical systems showing bistability is a challenging subject that has been a matter of study in molecular materials for device applications. When associated with a response function, for instance optical or magnetic, these systems can be used as memory devices, thermal sensors or switching units.[5] The nature of the transitions found in $(DT–TTF)_4[Au(pds)_2]_3$ is not completely clear yet. As in more general partially oxidized molecular systems, these phase transitions often result from a cooperative action of different mechanisms such as Peierls distortions, charge and anion ordering together with molecular distortions, and their relative role has been a matter of general debate with a more recent emphasis on charge ordering.[6]

All these facts prompted us to endeavor a systematic study of possible new anionic complexes related to $Au(pds)_2$, based for example on Au or Cu, and in similar selenated (pds) or sulfurated (pdt) ligands. Thus, the investigation on the chemical modifications of the anionic moiety in $(DT–TTF)_4[Au(pds)_2]_3$ led us to study the DT–TTF based radical ion salts formed with different transition metal complexes of similar size and shape, *i.e.* $[Cu(pds)_2]^-$,[7,8] $[Cu(pdt)_2]^-$,[7b,8] and $[Au(bdt)_2]^-$.[9] In the present work, we report on the structure

[a]*Departamento de Química, Instituto Tecnológico e Nuclear, CFMC-UL, P-2686-953 Sacavém, Portugal. E-mail: malmeida@itn.pt*
[b]*Institut de Ciència de Materials de Barcelona, Campus de la UAB, E-08193 Bellaterra, Spain. E-mail: cun@icmab.es*
[c]*Instituto de Telecomunicações and Departamento de Engenharia Química, Instituto Superior Técnico, P-1049-001 Lisboa, Portugal. E-mail: rth@ist.utl.pt*
[d]*Institut für Allgemeine, Anorganische und Theoretische Chemie, Universität Innsbruck, Innrain 52a, Innsbruck, Austria. E-mail: Klaus.Wurst@uibk.ac.at*
[e]*Laboratoire de Physique des Solides, Bâtiment 510, Univ. Paris-Sud, F-91405 Orsay, France. E-mail: foury@lps.u-psud.fr*

† Electronic supplementary information (ESI) available: X-ray crystallographic files for $(DT–TTF)_4[Au(pds)_2]_3$ (**1**), $(DT–TTF)_4[Cu(pds)_2]_3$ (**3**), $(DT–TTF)_4[Cu(pdt)_2]_3$ (**4**) and $(DT–TTF)[Cu(pdt)_2]$ (**5**) (CIF). Tables including short contacts of **1**, **3** and **4**, and list of selected bond distances within transition metal complexes in **1**, **3** and **4**. Full structural description of $(DT–TTF)[Cu(pdt)_2]$ (**5**). Oriented single crystal EPR measurements of **1–4**. See http://dx.doi.org/10.1039/b505724h

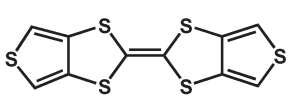

DT-TTF

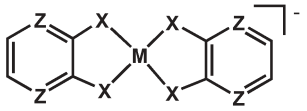

$Au(pds)_2^-$ (M = Au, X = Se, Z = N)
$Au(bdt)_2^-$ (M = Au, X = S, Z = CH)
$Cu(pds)_2^-$ (M = Cu, X = Se, Z = N)
$Cu(pdt)_2^-$ (M = Cu, X = S, Z = N)

Scheme 1

and properties of a new and large family of compounds with a 4 : 3 donor : acceptor stoichiometry (see Scheme 1), with closely related structures that reversibly interconvert at different temperature ranges, following a common pattern of phase transitions, along with the occurrence of electrical and magnetic bistability. In particular, we discuss the structural differences and similarities between the four compounds $(DT–TTF)_4[M(L)_2]_3$ (M = Au, Cu; L = pds, pdt, bdt), their physical properties, and the reversible phase transitions observed, which are related to variations from dynamic to static charge ordering.

Results and discussion

Synthesis

The compound $(DT–TTF)_4[Au(pds)_2]_3$ (**1**) was obtained by electrocrystallization and its synthetic details were reported elsewhere.[3] The other three compounds $(DT–TTF)_4[Au(bdt)_2]_3$ (**2**), $(DT–TTF)_4[Cu(pds)_2]_3$ (**3**) and $(DT–TTF)_4[Cu(pdt)_2]_3$ (**4**) were obtained by the same methodology and under similar experimental conditions. However, with the $Cu(pdt)_2$ anion another compound of different stoichiometry, (DT–TTF)-$[Cu(pdt)_2]$ (**5**), was also obtained in many electrocrystallizations under the same conditions, a phenomenon already observed in other DT–TTF salts.[2d]

Structural characterization

The crystal structure parameters of compounds **1–5** are listed in Table 1. For a more convenient discussion and comparison with the structures of compounds **2**, **3** and **4** reported in this paper, which are closely related to **1**, we start the structural description by summarizing the main structural features of **1**.[3]

$(DT–TTF)_4[Au(pds)_2]_3$ (1). The structure of **1** was determined at 293 K. This compound crystallizes in the triclinic system, space group $P\bar{1}$, and the asymmetric unit consists of two DT–TTF molecules and one and a half $Au(pds)_2^-$ units. Four DT–TTF units, related by an inversion center and stacked along the $a + b$-axis, form a so-called tetrad. The DT–TTF units within the tetrad are organized following the sequence DT1–DT2–DT2*–DT1*. The angle between the average plane of the DT–TTF units and the cell axis b is 83.6° for both DT1 and DT2 units. Each tetrad is flanked by two $Au(pds)_2$ complexes placed almost orthogonally and parallel to the long DT–TTF axis (AuSeComplex1 unit), and by another almost orthogonal $Au(pds)_2$ complex with the Au atom located at an inversion centre along the short DT–TTF axis (AuSeComplex2 unit) (see Fig. 1). The S···S intratetrads

Table 1 Crystal data and structure refinement of complexes **1–5**

	$[DT–TTF]_4[Au^{III}(pds)_2]_3$ (**1**)[b]	$[DT–TTF]_4[Au^{III}(bdt)_2]_3$ (**2**)[c]	$[DT–TTF]_4[Cu^{III}(pds)_2]_3$ (**3**)	$[DT–TTF]_4[Cu^{III}(pdt)_2]_3$ (**4**)	$(DT–TTF)[Cu^{III}(pdt)_2]$ (**5**)
Formula	$C_{64}H_{28}Au_3N_{12}S_{24}Se_{12}$	$C_{76}H_{40}Au_3S_{36}$	$C_{64}H_{28}Cu_3N_{12}S_{24}Se_{12}$	$C_{64}H_{28}Cu_3N_{12}S_{36}$	$C_{18}H_8CuN_4S_{10}$
Formula weight	3272.84	2698.14	2872.56	2309.76	664.42
Crystal system	Triclinic	Triclinic	Monoclinic	Monoclinic	Monoclinic
Space group	$P\bar{1}$	$P\bar{1}$	Cc	Cc	$P2_1/n$
a/Å	9.7118(9)	9.498(5)	32.8784(2)	32.5313(2)	11.8136(4)
b/Å	13.6202(10)	13.701(5)	9.6280(4)	9.4923(4)	10.5663(3)
c/Å	17.1685(15)	17.120(5)	26.7125(8)	26.3669(7)	18.5831(7)
α/°	97.254(6)	94.590(5)	90	90	90
β/°	106.132(7)	105.991(5)	98.853(2)	99.166(2)	101.834(2)
γ/°	95.956(7)	98.460(5)	90	90	90
V/Å^3	2141.1(15)	2101.3(15)	8355.2(4)	8038.0(4)	2270.35(10)
Z	1	1	4	4	4
D_c/g cm^{-3}	2.538	2.132	2.284	1.909	1.944
T/K	293(2)	200(2)	233(2)	233(2)	233(2)
λ/Å	1.54150 (Cu Kα)	0.71073 (Mo Kα)	0.71073 (Mo Kα)	0.71073 (Mo Kα)	0.71073 (Mo Kα)
μ/mm^{-1}	21.196	—	6.636	1.776	1.901
Reflections collected	8110	—	19 605	20 764	10 317
Independent reflections	7620 [R_{int} = 0.0523]	—	10 768 [R_{int} = 0.0588]	11 754 [R_{int} = 0.0488]	3143 [R_{int} = 0.0537]
GOF on F^2	0.971	—	1.023	1.023	1.105
R/R_w[a]	0.0701/0.1602	—	0.0496/0.0888	0.0418/0.0761	0.0508/0.1252

[a] $R = \Sigma||F_o| - |F_c||/\Sigma|F_o|$ and $R_w = \{\Sigma[w(F_o^2 - F_c^2)^2]/\Sigma[w(F_o^2)^2]\}^{1/2}$ where $w = 1/[\sigma^2(F_o^2 + (aP)^2 + bP]$, $P = (F_o^2 + 2F_c^2)/3$, and a and b are constants given in the electronic supplementary information (ESI). [b] See complete crystallographic description in ref. 3. [c] Poor diffraction data set only allowed for the determination of the crystal cell parameters, but not for a good refinement of the structure.

contacts vary from 3.46 to 3.69 Å, whereas the end DT–TTF units of each tetrad are connected to two other tetrads through S···S contacts ranging from 3.83 to 4.13 Å, as shown in Fig. 1b,

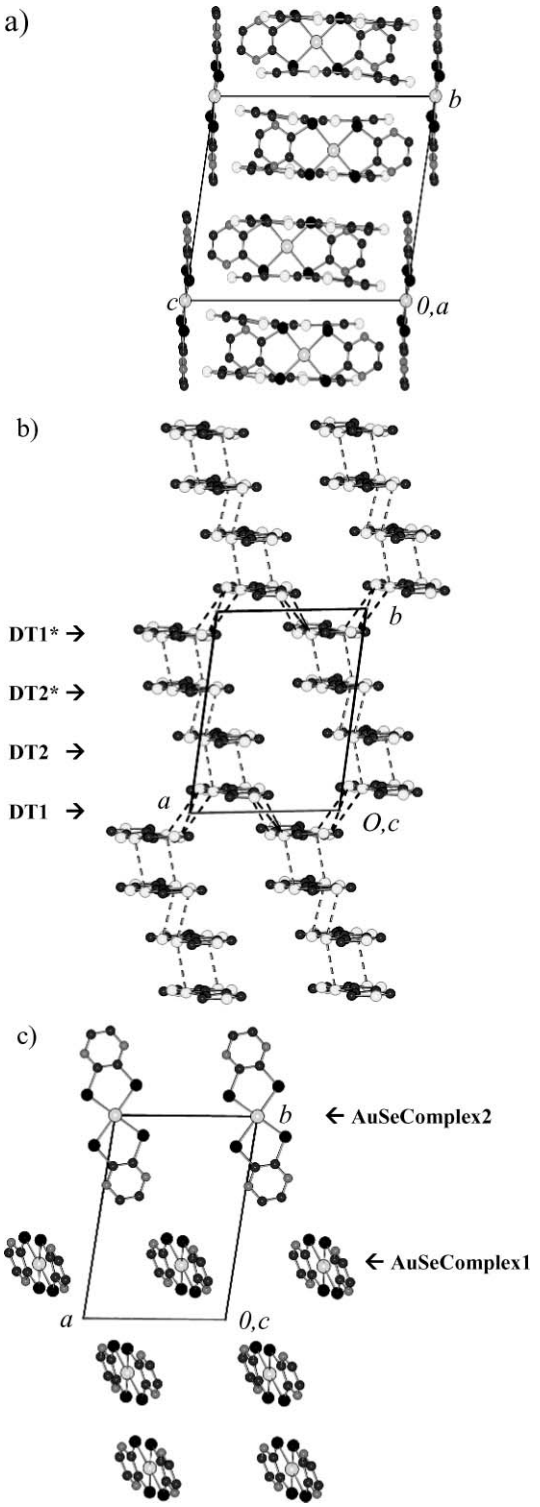

Fig. 1 (a) Crystal structure of $(DT–TTF)_4[Au(pds)_2]_3$ (**1**) at 293 K, viewed along the *a*-axis; (b) view of the DT–TTF sublattice along the *c*-axis (anions were omitted for clarity and the doted lines indicate short S···S contacts) and (c) view of the anions sublattice along the *c*-axis. Data from ref. 3.

where only the DT–TTF network viewed along the *c*-axis is represented.[3] The four DT–TTF units of each tetrad present slightly different bond distances (see Table 2). The gold-containing anion sublattice viewed along *c* is depicted in Fig. 1c, showing the relative orientation between AuSeComplex1 and AuSeComplex2 units (the dihedral angle between the latter and the *a*,*b* plane is 9.85°). A list of selected bond distances in the anionic units, as well as a list of S···S, Au···S and Se···S contact distances, can be found in the electronic supplementary information (ESI)†. The crystal cell then contains four DT–TTF and three $Au(pds)_2$ units.

$(DT–TTF)_4[Au(bdt)_2]_3$ (2). The structure of **2** was determined at 200 K. Compound **2** crystallizes in the triclinic system, space group $P\bar{1}$, being isostructural to the other gold compound **1** (see Table 1 and Fig. 1). Due to lower crystal quality, the structure could only be resolved with a high agreement factor (R = 0.2030), which is enough to conclude that **2** is isostructural to **1**, with the same packing pattern, as shown in Fig. 2, but not sufficient for a more precise analysis of bond distances and contacts.

$(DT–TTF)_4[Cu(pds)_2]_3$ (3) and $(DT–TTF)_4[Cu(pdt)_2]_3$ (4). The structures of **3** and **4** were determined at 233 K, in all cases

Table 2 Selected bond distances (in Å) in the DT–TTF asymmetric units for compounds **1**, **3**–**4**

Atoms	Distance	Atoms	Distance
$(DT–TTF)_4[Au(pds)_2]_3$ (1)			
DT1 unit		**DT2 unit**	
C13–C14	1.36(2)	C23–C24	1.36(2)
C13–S4	1.744(17)	C23–S10	1.713(17)
C13–S5	1.741(17)	C23–S11	1.758(19)
C14–S1	1.746(18)	C24–S7	1.754(19)
C14–S2	1.730(17)	C24–S8	1.747(18)
$C–S_{average}$	1.740	$C–S_{average}$	1.743
$(DT–TTF)_4[Cu(pds)_2]_3$ (3)			
DT1 unit		**DT3 unit**	
C25–C30	1.372(17)	C45–C50	1.345(14)
C25–S1	1.740(12)	C45–S13	1.757(11)
C25–S3	1.745(12)	C45–S15	1.749(12)
C30–S4	1.725(12)	C50–S16	1.739(11)
C30–S6	1.733(12)	C50–S18	1.761(11)
$C–S_{average}$	1.736	$C–S_{average}$	1.752
DT2 unit		**DT4 unit**	
C35–C40	1.358(16)	C55–C60	1.328(16)
C35–S7	1.737(16)	C55–S19	1.745(12)
C35–S9	1.751(12)	C55–S21	1.754(12)
C40–S10	1.757(12)	C60–S22	1.773(12)
C40–S12	1.716(12)	C60–S24	1.748(12)
$C–S_{average}$	1.740	$C–S_{average}$	1.755
$(DT–TTF)_4[Cu(pdt)_2]_3$ (4)			
DT1 unit		**DT3 unit**	
C25–C30	1.395(9)	C45–C50	1.361(9)
C25–S1	1.734(6)	C45–S13	1.746(6)
C25–S3	1.717(6)	C45–S15	1.752(7)
C30–S4	1.730(7)	C50–S16	1.763(6)
C30–S6	1.729(6)	C50–S18	1.741(6)
$C–S_{average}$	1.728	$C–S_{average}$	1.751
DT2 unit		**DT4 unit**	
C35–C40	1.374(10)	C55–C60	1.355(9)
C35–S7	1.725(7)	C55–S19	1.749(6)
C35–S9	1.732(7)	C55–S21	1.746(6)
C40–S10	1.739(6)	C60–S22	1.753(7)
C40–S12	1.734(7)	C60–S24	1.739(6)
$C–S_{average}$	1.733	$C–S_{average}$	1.747

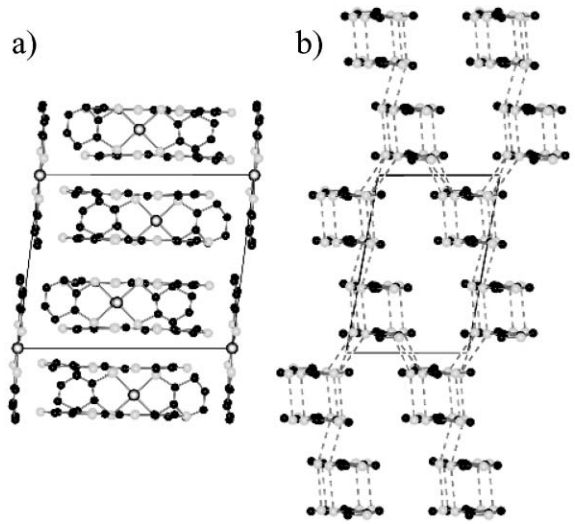

Fig. 2 Crystal structure of $(DT–TTF)_4[Au(bdt)_2]_3$ (**2**) at 200 K viewed along: (a) the *c*-axis; (b) the *a*-axis with anions omitted for clarity and the dotted lines indicate S···S contacts.

above the first-order structural phase transitions of these compounds, as described below. Both compounds are isostructural and the structural description of **3** also applies for **4**; therefore, the corresponding structural data for **4** will be indicated in brackets hereafter. Compounds **3** and **4** crystallize in the monoclinic system, space group *Cc*, with an asymmetric unit containing four independent DT–TTF units and three $Cu(pds)_2$ complexes, all located in general positions. These units are packed in a similar manner as in **1**, but the unit cell is now doubled along two axes and there is a significantly different relative displacement of the third DT–TTF molecule of each tetrad (see Fig. 3). DT–TTF molecules are labeled as DT1, DT2, DT3 and DT4 units, consecutively. Units 1, 3 and 4 present a small boat distortion with the outer sulfur atoms deviated towards outside the tetrad. The deviations of the outer sulfur atoms from the average plane of the molecules are of −0.186 [−0.162] Å and −0.206 [−0.158] Å for S2 and S5 in DT1 unit, 0.097 [0.096] Å and 0.093 [0.112] Å for S14 and S17 in DT3 unit, and 0.159 [0.154] Å and 0.176 [0.152] Å for S20 and S23 in DT4 unit. On the other hand, the DT2 unit is almost planar (rms deviation of fitted atoms = 0.037 [0.032] Å). The four DT–TTF units of each tetrad present slightly different bond distances (see Table 2).

Indeed, the stacking motif within each tetrad is different from the gold analogue $(DT–TTF)_4[Au(pds)_2]_3$ (**1**), since the DT3 unit severely disrupts the otherwise smooth and uniform slipping along the short axis of these units. The distance between average planes of DT1–DT2 is 3.31 [3.03] Å, 3.19 [3.21] Å between DT2–DT3 and 4.02 [4.07] Å between DT3–DT4.[10] The angles of the average plane of DT–TTF units and the cell axis *c* are 86.4° [86.1°] for DT1, 84.1° [82.6°] for DT2, 83.2° [81.5°] for DT3 and 86.7° [85.7°] for DT4 unit. It should be noted that the latter angles are slightly smaller for **3**, and therefore, an increased tilt angle of the DT–TTF molecular plane along the stacking axis *c* is noticed.

The end units of the tetrads DT1 and DT4, are connected to two other tetrads by Se···Se [S···S] contacts forming a bidimensional network of short interdonor Se···Se [S···S] contacts in the *c*,*b* plane. These donor tetrads, stacked along *c* + *b*, are flanked by two $Cu(pds)_2$ units: CuSeComplex1 [CuSComplex1] unit is flanking DT1 and DT2 units with an angle between the average planes of these DT units and the mean plane of the anion unit of 75° [75°].[11] On the other hand, CuSeComplex2 [CuSComplex2] unit is flanking DT3 and DT4

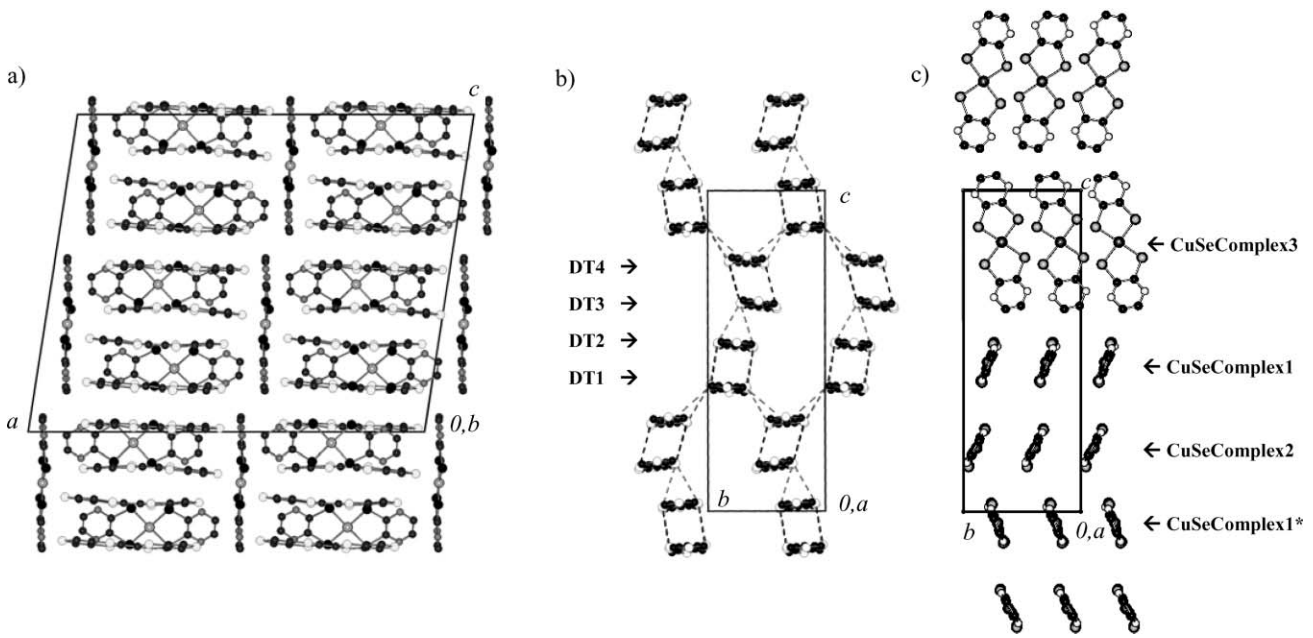

Fig. 3 (a) Crystal structure of $(DT–TTF)_4[Cu(pds)_2]_3$ (**3**) at 233 K viewed along the *b*-axis; (b) partial view along the *c*-axis (only one sheet is shown) where the anions were omitted for clarity and the dotted lines indicate short S···S contacts; (c) partial view along the *c*-axis of the anions (the DT–TTF molecules were omitted for clarity).

units with an angle between the mean planes of these DT units and the mean plane of the anion unit of 59° [58°],[11] CuSeComplex2 [CuSComplex2] tilted by 45.8° [46.2°] with respect to CuSeComplex1 [CuSComplex1] unit (see Fig. 3). The third non-equivalent copper complex of the asymmetric unit is labeled as CuSeComplex3 [CuSComplex3] units, and it is found flanking two dimers of DT–TTF of different tetrads (see Fig. 3a). Along the *a*-axis, these donors alternate with layers of [Cu(pds)$_2$] (CuSeComplex3 unit) [[Cu(pdt)$_2$] (CuSComplex3 unit)] which lie almost parallel to the *c*,*b* plane, with an angle of 8.5° [8.8°].

The bond lengths of the DT–TTF units in **4**, as shown in Table 2, suggest a charge separation with DT1 and DT2 units presenting higher charge than DT3 and DT4, in agreement with the electronic structure calculations discussed below. Such a conclusion cannot be drawn so clearly for **3** due to the lower reliability of the structure refinement. In this respect it is worth noting that structural data for compound **1** do not show any clear sign of such localisation.

Selected bond distances of the anionic moieties for **3** and **4** can be found in the ESI†. The crystal cells of **3** and **4** are four times larger than in **1** and **2**, and they include a total of 16 DT–TTF and 12 Cu(pds)$_2$ [Cu(pdt)$_2$] molecules. The main difference between the structures of compounds **3** and **4** is an increased modulation among the DT–TTF tetrads of the tilt angle of the donors relative to the *c*-axis in **4**.

(DT–TTF)[Cu(pdt)$_2$] (5). Compound **5** crystallizes as dark pink shining plates and was obtained under the same conditions as **4**, and usually each crystallization batch yielded a mixture of both. It crystallizes in the monoclinic system, space group $P2_1/n$ (T = 233 K), with an asymmetric unit containing one independent DT–TTF and one Cu(pdt)$_2$ units in general positions. This 1 : 1 stoichiometric salt is characterized by the dimerization of both the DT–TTF units and the Cu(pdt)$_2$ units, in such a way that alternating layers of anions and cations are formed along the *b*-axis. A full structural description of this compound can be found in the ESI†.

Electrical transport measurements

The electrical conductivity, σ, and thermopower, S, of (DT–TTF)$_4$[Au(pds)$_2$]$_3$ (**1**) measured in single crystals have been already reported, with room temperature values σ_{RT} = 2 S cm^{-1} and S_{RT} = −60 μV K^{-1}.[3] In both transport properties, a sharp second-order phase transition at T_{c1} = 238 K is observed, whereas upon further cooling, a first-order transition with a large hysteresis in the range T_{c2} = 120–200 K was also observed (see Figs. 4 and 5).

The electrical conductivity of (DT–TTF)$_4$[Au(bdt)$_2$]$_3$ (**2**) has a room temperature value of σ_{RT} = 3 S cm^{-1} (E_a = 76 meV), showing a second-order phase transition at 183 K, which resembles the features of **1** near the upper phase transition (see Fig. 4). However, at variance with **1**, no first-order transition is detected in **2** at lower temperatures down to 90 K. At room temperature the thermopower is negative, $S_{RT} \approx -60$ μV K^{-1}, presenting an almost temperature-independent behavior down to 183 K, also very similar to **1** above the high temperature phase transition. It is worth noting that this value of thermopower is close to the spin entropy contribution $-(k_B/|e|)$ ln 2 = −59.8 μV K^{-1} expected for strongly-correlated half-filled band systems.[12]

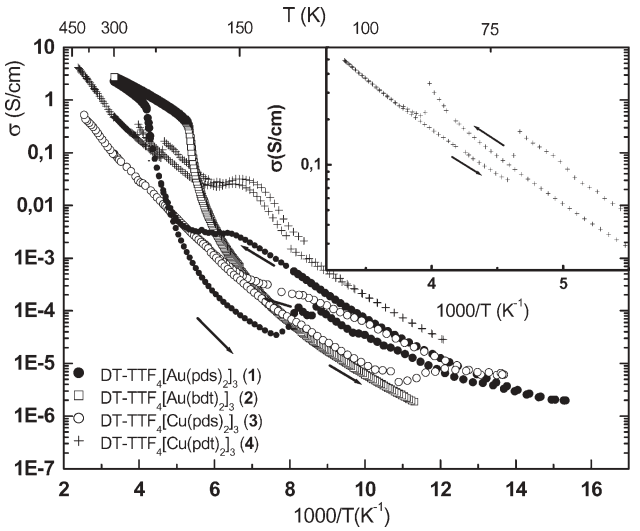

Fig. 4 Electrical conductivity, σ, of compounds **1**–**4** as a function of the inverse temperature. The inset shows in detail the hysteresis of **4** around the phase transition.

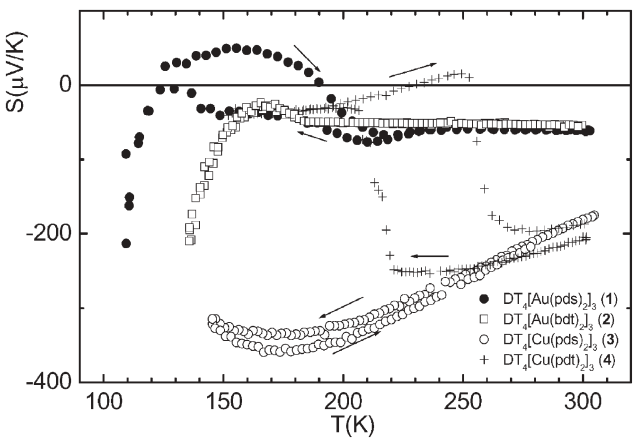

Fig. 5 Absolute thermopower, S, of compounds **1**–**4** as a function of temperature, T.

The measurements performed on (DT–TTF)$_4$[Cu(pds)$_2$]$_3$ (**3**) revealed a different situation compared to the gold analogue **1** (see Fig. 4). The room temperature value of electrical conductivity is σ_{RT} = 0.1 S cm^{-1}, more than one order of magnitude lower than in **1**. Furthermore, no sharp second-order phase transition was found upon cooling. However, a first-order transition with a large hysteretic loop, similar to **1** but at lower temperatures, is found in the range 80–150 K.[8] Thus, upon cooling, the electrical conductivity showed at ∼80 K a transition towards a higher conductivity semiconducting phase, with approximately the same activation energy.

The thermoelectric power of **3** at room temperature is S_{RT} = −180 μV K^{-1}, following a typical semiconducting behavior with absolute values increasing upon cooling and with a large but smooth hysteresis between 140 and 250 K (see Fig. 5).

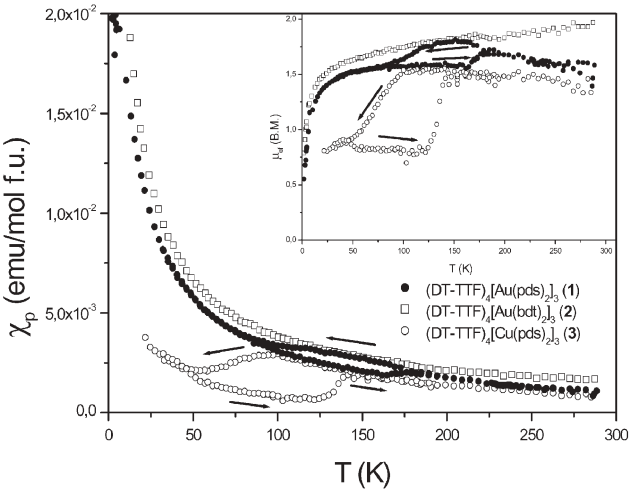

Fig. 6 Paramagnetic susceptibility of **1**–**3** as a function of temperature. The inset shows the corresponding effective magnetic moment.

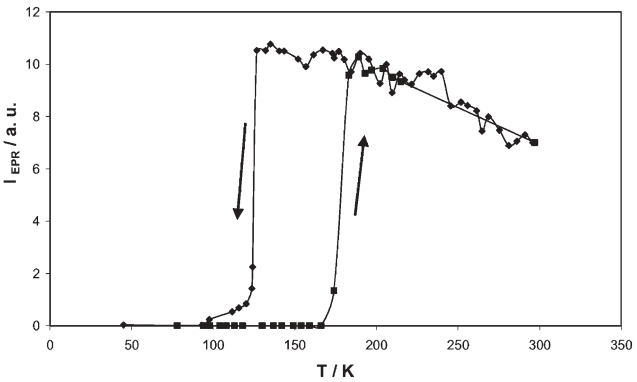

Fig. 7 EPR signal intensity of $(DT–TTF)_4[Au(pds)_2]_3$ (**1**) as a function of temperature.

The electrical conductivity of $(DT–TTF)_4[Cu(pdt)_2]_3$ (**4**), $\sigma_{RT} = 0.5$ S cm^{-1}, is between that of **1** and **3**, with a semiconducting behavior as in **3**, and showing only one first-order phase transition, but with a weaker hysteresis, in the range 125–260 K (Fig. 4).[8] The hysteresis shape is peculiar in the sense that the cooling and warming directions of cycle cross with each other, which is likely due to induced microcracking and not so different conductivity values are found in the lower and higher temperature ranges. A reproducible anomaly between ~154–170 K is also noticed, seen as a bump in the electrical conductivity in both the cooling and warming directions. The conductivity measurements of **3** and **4** were extended above room temperature up to near the decomposition temperature (~360 K), but no sign of any additional phase transition was found.

The thermoelectric power at room temperature of **4** is $S_{RT} = -190$ μV K^{-1}, comparable to **3** and following a similar semiconducting behavior (Fig. 5). The first-order transition is clearly seen as a large hysteretic loop between 210–270 K, but with no sign of the bump anomaly observed in resistivity around 150–170 K.

Magnetic measurements

The paramagnetic molar susceptibility (χ_p) *versus* temperature exhibited by compound $(DT–TTF)_4[Au(pds)_2]_3$ (**1**) indicated a Curie–Weiss behavior with a room temperature $\chi_p = -1.09 \times 10^{-5}$ emu mol^{-1}.[3] The cooling and warming measurements of susceptibility showed a weak hysteresis in the range 80–180 K (Fig. 6), which approximately overlaps with the first-order phase transition observed in the electrical transport properties. The small temperature differences between the different measurements are certainly related to different cooling/heating rates employed in different experiments. However in the magnetic susceptibility measurements of **1**, no variation was detected around 238 K, the temperature where a sharp second-order transition was clearly observed on the conductivity measurements. The EPR signal intensity *versus* temperature obtained by a complete EPR study on an oriented single crystal agrees with the susceptibility measurements (Fig. 7). Notably, a sharp and clear transition with a large decrease of the spin susceptibility associated with a hysteresis is observed in the same temperature range as the one in the static susceptibility (χ_p) *versus* temperature plot (Fig. 6). Nevertheless, there is a difference between the magnitude of the drop of susceptibility in both measurements that can be attributed to the fact that in EPR, below the transition, there is a very weak and wide signal difficult to integrate. It is also possible that not all crystals in the bulk sample have the same quality and do not undergo the transition as the selected crystal used in the EPR studies. The sudden drop of EPR signal is probably caused by a strong dimerization, and therefore making this material suitable for a magnetic device with potential applications as a thermal sensor or a switching unit.[5] The three g values found for the different orientations of the crystal (g_{max} when H//long axis of the molecule, g_{med} when H//short axis of the molecule, and g_{min} when H $\perp$ plane of the molecule) are in accordance with the orientation of the DT–TTF molecules in the crystal (see Table 3).

The magnetic susceptibility behavior of **2** is different than the other compounds of this family since no first-order transition is observed at low temperature (Fig. 6). Considering a diamagnetic contribution, estimated from Pascal constants, of $\chi_d = -10.01 \times 10^{-4}$ emu mol^{-1}, the paramagnetic susceptibility at room temperature is $\chi_p = 16.90 \times 10^{-4}$ emu mol^{-1},

Table 3 EPR data of oriented crystals at room temperature

	$DT_4(Au(pds)_2)_3$ (**1**)	$DT_4(Au(bdt)_2)_3$ (**2**)	$DT_4(Cu(pds)_2)_3$ (**3**)	$DT_4(Cu(pdt)_2)_3$ (**4**)
g_{max} (ΔH_{pp} (G)) H//j^a	2.0092 (20.2)	2.0089 (16.2)	2.0112 (15.3)	2.0123 (1.52)
g_{med} (ΔH_{pp}(G)) H//i^a	2.0052 (15.9)	2.0040 (20)	2.0068 (9.72)	2.0061 (1.20)
g_{min} (ΔH_{pp}(G)) H//k^a	2.0006 (16.7)	1.9998 (14.4)	2.00020 (10)	2.00015 (1.17)

[a] For compounds **1** and **2** the *j*, *i* and *k* axes correspond to the crystallographic *c*, *a* and *b* axes, respectively. On the other hand, for compounds **3** and **4** the *j*, *i* and *k* axes correspond to the crystallographic *a*, *b* and *c* axes, respectively.

only slightly larger than that of the isostructural compound **1**, and increases upon cooling approximately following a Curie–Weiss law with an effective magnetic moment of 1.9 μ_B. The second-order transition at 183 K is barely seen as in the case of compound **1**. Nevertheless, this transition is clearly observed in the EPR measurements (see ESI† and Table 3).

The paramagnetic molar susceptibility (χ_p) *versus* temperature of a bulk polycrystalline sample of compound (DT–TTF)$_4$[Cu(pds)$_2$]$_3$ (**3**), considering a diamagnetic contribution estimated from Pascal constants of $\chi_d = 8.26 \times 10^{-4}$ emu mol^{-1}, is plotted in Fig. 6. The room temperature paramagnetic susceptibility is $\chi_p = 4.14 \times 10^{-4}$ emu mol^{-1}, with a clear hysteretic loop generated from the cooling and warming experiments in the range 50–145 K, hysteresis comparable to that observed in the electrical transport measurements. The EPR experiments performed on an oriented single crystal yielded the same behavior for the EPR signal intensity *versus* temperature (see Table 3 and ESI†).

Due to the difficulty in harvesting enough quantity of crystalline material to measure the static paramagnetic susceptibility on a bulk sample of (DT–TTF)$_4$[Cu(pdt)$_2$]$_3$ (**4**), their magnetic properties were studied only by EPR measurements on an oriented single crystal with the magnetic field parallel to the shortest axis of the crystal (that corresponds to the *c*-axis, since the same indexation of the crystal as in **3** is found), (see Table 3 and ESI†). The EPR signal intensity *versus* temperature plot, depicted in Fig. 8, shows a sharp phase transition associated with a hysteretic loop in the range between 200 and 260 K. This hysteresis was also observed on the electrical transport measurements as mentioned in the previous section. The sudden EPR intensity drop, that is probably due to a strong dimerization, make this material suitable for a possible magneto-thermal switch device,[5] similarly to compound **1**.

The EPR measurements of **3** and **4** were extended to higher temperatures (400 K) to look for any sign of transition. While no change of the EPR intensity slope was observed for **3** (see ESI†), we did observe a shallow slope inflexion at 320 K for compound **4** (Fig. 8). However, X-ray diffraction studies above and below 320 K discarded any structural modification.

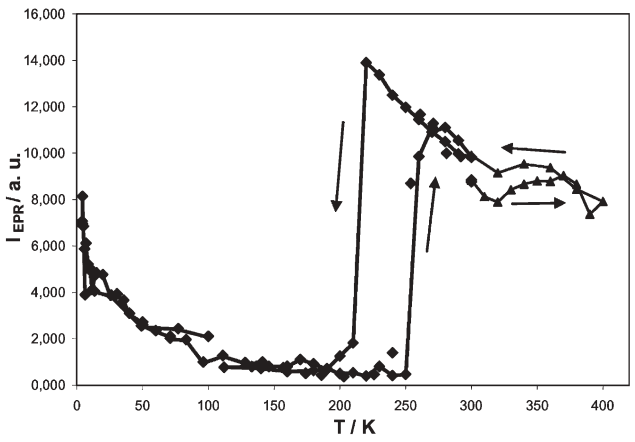

Fig. 8 EPR signal intensity of (DT–TTF)$_4$[Cu(pdt)$_2$]$_3$ (**4**) as a function of temperature.

Compound **5** was found to be EPR silent, a fact that is ascribed to the strong dimerization of the spin carrying units, the DT–TTF donors.

Diffuse X-ray scattering studies: interconnection between phases

In order to enlighten the nature of the phase transitions observed in the electrical and magnetic measurements, variable-temperature single crystal X-ray measurements were attempted for all the (DT–TTF)$_4$[M(L)$_2$]$_3$, or DT$_4$M$_3$ for short, compounds using conventional automated diffractometers. In the case of (DT–TTF)$_4$[Au(pds)$_2$]$_3$ (**1**), apart from a very large line broadening of the reflections, no significant changes in the unit cell parameters were detected at temperatures below the second-order transition at T_{c1} = 238 K. Similarly, crystals of (DT–TTF)$_4$[Cu(pds)$_2$]$_3$ (**3**) did not diffract well at temperatures below the hysteresis loop (45 K). Finally, the higher mosaicities found by lowering the temperature below the sharp transition observed in (DT–TTF)$_4$[Cu(pdt)$_2$]$_3$ (**4**) prevented the collection of any data. Only in the case of (DT–TTF)$_4$[Au(bdt)$_2$]$_3$ (**2**), using a diffractometer with an image plate, was it possible to clearly observe the doubling of the unit cell along *b* at 130 K, well below the second-order transition at 183 K (see Table 4). However, as in other cases, the poor diffracting quality prevented the refinement of the full structure.

Therefore we decided to study these compounds using the so-called fixed film–fixed crystal method and monochromated Cu Kα (λ = 1.542 Å) radiation as in previous studies on (DT–TTF)$_2$M(mnt)$_2$ compounds.[2c,d] This technique can easily detect small changes in the diffraction pattern and the eventual presence of diffuse scattering related to pre-transitional structural fluctuations.

Crystals of (DT–TTF)$_4$[Au(pds)$_2$]$_3$ (**1**) below the transition at T_{c1} = 238 K, showed the appearance of new satellite spots at the reduced wave vector $q = b^*/2 + c^*/2$, which correspond to a duplication of the lattice in the *b* and *c* directions (Fig. 9).[8] This new unit cell has dimensions almost identical to the unit cells of **3** and **4**. No precursor effect associated to this transition has been detected above T_{c1}. Well below $T_{c2} \sim 150$ K, X-ray diffraction patterns showed additional changes (Fig. 10), which are mainly characterized by the appearance of new satellite reflections located at q = (?, $b^*/4$, ?) (using the room temperature crystallographic parameters). This corresponds to a new duplication of the lattice along *b*. The intensity of the additional reflections is quite strong suggesting that this transition involves significant structural modifications.

Table 4 Crystallographic data for compound (DT–TTF)$_4$[Au(bdt)$_2$]$_3$ (**2**) at 200 and 130 K

ML$_2$	Au(bdt)$_2$	Au(bdt)$_2$
T/K	200	130
Space group	$P\bar{1}$	$P\bar{1}$
a/Å	9.4980(14)	9.482
b/Å	13.7007(31)	27.243
c/Å	17.1197(23)	17.104
α/°	94.588(23)	94.765
β/°	105.991(17)	97.974
γ/°	98.456(23)	105.990
V/Å^3	2101.2(6)	4171.9

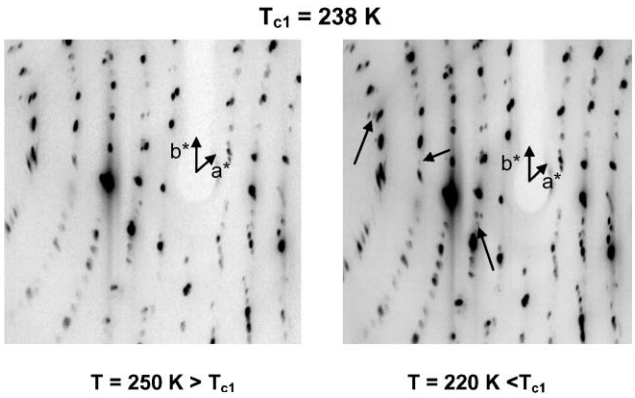

Fig. 9 X-Ray pattern of a single crystal of $(DT–TTF)_4[Au(pds)_2]_3$ (**1**) above and below the high temperature phase transition T_{c1}. The superstructure reflections are indicated by arrows.

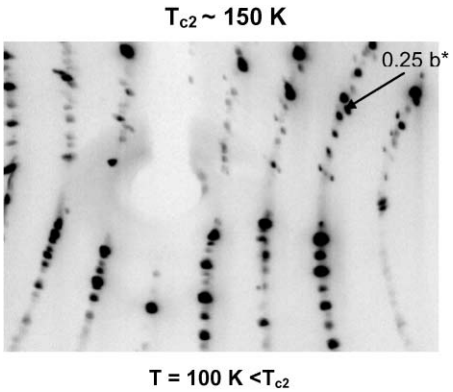

Fig. 10 X-Ray pattern of a single crystal of $(DT–TTF)_4[Au(pds)_2]_3$ (**1**) below the low temperature phase transition T_{c2}. The superstructure reflections are indicated by arrows.

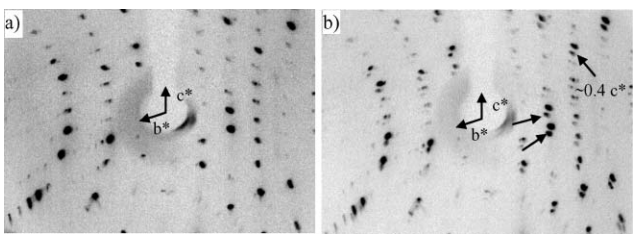

Fig. 11 X-Ray pattern of a single crystal of $(DT–TTF)_4[Cu(pds)_2]_3$ (**3**) at T = 200 K (a) and T = 150 K (b), respectively above and below the transition temperature $T_c \sim 200$ K. The superstructure reflections are indicated by arrows.

For the Cu analogue, $(DT–TTF)_4[Cu(pds)_2]_3$ (**3**), large changes in the X-ray diffraction patterns were observed between 200 and 150 K. This indicates large structural modification similar to that observed in the $Au(pds)_2$ compound below T_{c2} (Fig. 11). However in this Cu system, the satellite spots are located at q = (?, ?, 0.4c*), indicating that the structural modulation is incommensurate (note that the c* and b* parameters are inverted between the **1** and **3** compounds).

The full structural refinement of the four compounds in their different phases is necessary to clarify the pattern of phase transitions between these closely related structures. In view of the previous data one possible interpretation of the high temperature second-order transition in the $(DT–TTF)_4[Cu(pds)_2]_3$ (**3**) system could be a charge ordering phenomena.

General discussion

In an attempt to find how the previous structural and physical information can be correlated we performed tight-binding band structure calculations on the basis of the X-ray structures determined for $(DT–TTF)_4[Au(pds)_2]_3$ (**1**) and $(DT–TTF)_4[Cu(pds)_2]_3$ (**3**) above any transition. The donor lattice of **1** can be described as being built from tetrads containing four different types of donor–donor interactions: two of them are intratetrad interactions and two are intertetrad interactions (see Fig. 1). Note that because of the symmetry the two outer interactions within the tetrads (*i.e.*, DT1–DT2 and DT1*–DT2*, see Fig. 1b) are identical whereas the inner one (*i.e.*, DT2–DT2*) is different. A simple and convenient way to evaluate the strength of the different HOMO···HOMO interactions in a lattice is by calculating the so-called $\beta_{HOMO–HOMO}$ interaction energies.[13] In the present case the two intratetrad interactions are 0.489 and 0.040 eV for the outer and inner interactions respectively (Table 5). The two intertetrad interactions are 0.046 and 0.086 eV. These values suggest that these tetrads should be considered as made of two dimers. The calculated band structure is reported in Fig. 12a and completely substantiates this analysis. The four bands in this figure appear as two pairs of bands separated by a relatively large gap which is mainly imposed by the dimerization strength and the energetic separation between the two bands of each pair is much weaker because the interdimer interactions are considerably smaller. In other words, the band structure of Fig. 12a corresponds to a lattice of dimers with quite modest interaction. The large difference between the two different intratetrad interactions can be easily understood by just looking at the corresponding overlap modes (see Figs. 12b and 12c where the two interactions have been labelled as intradimer and interdimer).

Before discussing the implications of these results let us consider the case of salt **3**. The repeat unit of the layer now contains two identical tetrads. However, the two dimers forming the tetrad are no longer symmetrically equivalent. Thus, there are two different intradimer interactions and one interdimer interaction per tetrad unit. The absolute values of the $\beta_{HOMO–HOMO}$ interaction energies are 0.688, 0.195 and 0.092 eV, respectively (Table 5). The two different intertetrad interactions are 0.070 and 0.081 eV. As for **1** all interdimer interactions are weak; what distinguishes the two salts is that for **3** the two dimers are very different, one having stronger

Table 5 Transfer integrals $|\beta_{HOMO–HOMO}|$ for compounds **1** and **3**

	$\lvert\beta_{HOMO–HOMO}\rvert$/eV	
Interactions	$(DT–TTF)_4[Au(pds)_2]_3$ (**1**)	$(DT–TTF)_4[Cu(pds)_2]_3$ (**3**)
Intradimer	0.489	0.688; 0.195
Interdimer (within tetrads)	0.040	0.092
Interdimer (between tetrads)	0.046; 0.086	0.070; 0.081

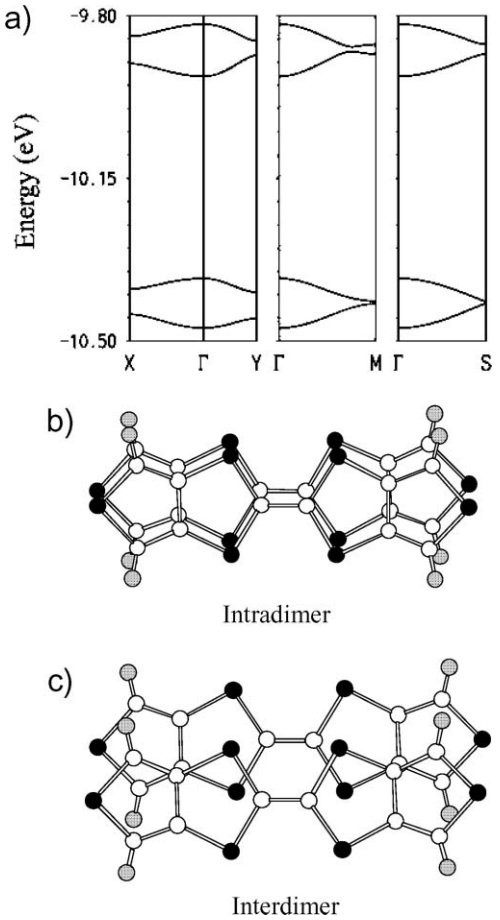

Fig. 12 (a) Calculated band structure for the donor layers in (DT–TTF)$_4$[Au(pds)$_2$]$_3$ (**1**) where Γ = (0, 0), X = (a*/2, 0), Y = (0, b*/2), M = (a*/2, b*/2) and S = (−a*/2, b*/2). (b) and (c) show the two different overlap modes within the tetrads units in these layers.

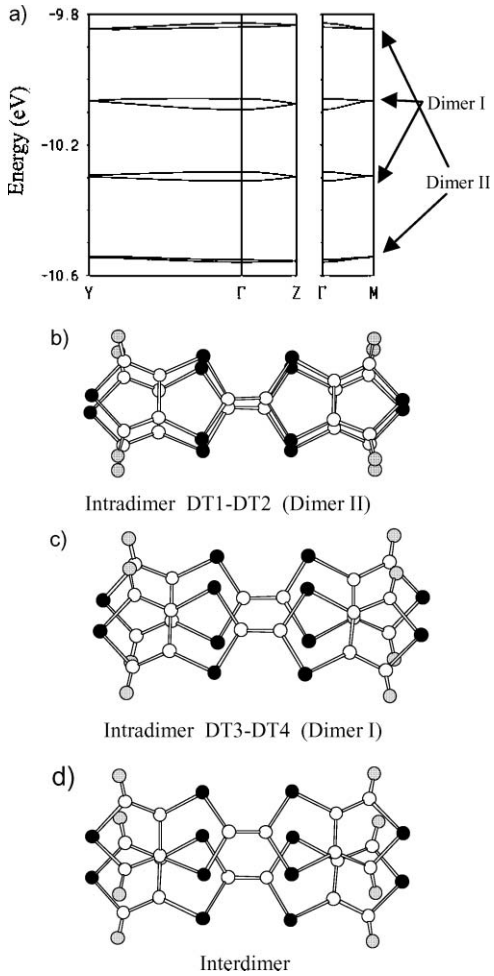

Fig. 13 (a) Calculated band structure for the donor layers in (DT–TTF)$_4$[Cu(pds)$_2$]$_3$ (**3**) where Γ = (0, 0), Y = (b*/2, 0), Z = (0, c*/2) and M = (b*/2, c*/2). (b), (c) and (d) show the three different overlap modes within the tetrads units in these layers.

intradimer interactions while the other has clearly weaker interactions than those found in **1**. The calculated band structure (see Fig. 13a) very nicely reflects this analysis. The eight bands (remember that now there are eight donors in the repeat unit) appear as four pairs of bands, the upper and lower ones being made of the HOMOs of one of the dimers (DT1–DT2 in Fig. 3b, dimer II in Fig. 13) and the two middle pairs being made of the HOMOs of the other dimer (DT3–DT4 in Fig. 3b, dimer I in Fig. 13). The respective energy band separations are just a measure of the different dimerization strength. Again, the difference between the different interactions within the tetrads can be easily understood by looking at the corresponding overlap modes (see Figs. 13b–d). Both the sliding along the short molecular axis and the larger interplanar distance contribute to the considerably weaker dimerization strength of the DT3–DT4 dimer. The weaker interdimer interaction despite a smaller interplanar separation is due to the worst orbital orientation clearly visible in Fig. 13d which decreases the σ component of the interaction.

Consequently, as far as the HOMO···HOMO interactions are concerned the two salts can be described as a series of dimeric units; identical in **1** but different in **3**. Compound **2** is isostructural to **1**, and compound **4** is found to be isostructural to compound **3** so that the same description is expected to be valid for the two gold compounds as well as for the two copper ones. Because of the peculiar 4 : 3 stoichiometry, the bands in Fig. 13a should house six holes so that the upper pair is completely empty and the second upper pair contains two additional holes. This means that of the three holes per tetrad unit, two are located in dimer II and one in dimer I. In other words, DT1 and DT2 can be described as (DT–TTF)$^+$ whereas DT3 and DT4 can be described as (DT–TTF)$^{+1/2}$. The question is less clear for the gold salts. The upper pair of bands in Fig. 12a must contain three holes. However, this means that three holes are distributed between two symmetrically equivalent dimers, a notion which at first sight may look as somewhat disturbing. Trying to keep all the structural and transport results in mind a clear difference among the gold and copper salts appears: the gold salts clearly exhibit a second-order transition at relatively high temperature leading to a structure of the same type as that of the copper salts, and this transition is clearly associated with a change in the transport properties. If we now realize that (i) the disappearance of the equivalence among the two dimers of the tetrad

leads to a perfectly comfortable description of the electronic structure, and (ii) for the two gold salts **1** and **2** there are two gold complexes of one type (AuSeComplex1/AuSComplex1 units) and one of a different type (AuSeComplex2/AuSComplex2 units) (see Fig. 1), it could be naïvely thought that the transition is associated with a change in the charges of the gold complexes so that before the transition two of them bear a negative charge while the other one is neutral, whereas after the transition all complexes bear a negative charge. Of course this would lead to two $(DT–TTF_2)^+$ dimers before the transition but to one $(DT–TTF_2)^+$ and one $(DT–TTF_2)^{2+}$ after the transition. However this suggestion implies that during the electrocrystallization process one gold complex is oxidized, something clearly unacceptable from the electrochemical viewpoint.[7,14] In view of the narrow bands and weak interdimer interactions, the uniform distribution of positive charge among the donors in **1**, and the relatively high electrical conductivity of this compound at room temperature are seen as an indication of a fast hopping regime of the electrons between dimers. According to this picture the second-order phase transition of **1** and **2**, where there is a sudden drop of electrical conductivity upon cooling, can correspond to the freezing of this hopping, towards a charge-ordered state with doubling of the cell parameters, probably with a structure similar to those of **3** and **4**. At this point it should be noted that the transition of the gold compound **1** at 238 K from a triclinic to a monoclinic space group along with the doubling of two unit cell axes with the same crystal packing observed in **3** and **4**, involves a severe rearrangement of the anion and DT–TTF molecules. The fact that the transition observed is second-order may indicate that the rearrangement does not lead to the same monoclinic crystal packing as in **3** or **4**, as it is indeed suggested by the different EPR behavior (see ESI†).

At lower temperatures, the gold compound **1** undergoes another phase transition (with hysteresis) that is related to another doubling of one of the axes of the crystal cell. This hysteretic transition is observed at different temperatures for the two copper systems **3** and **4**, a difference that is related to the chalcogen atom substitution. However, the latter transition is incommensurate for the $Cu(pds)_2$ system **3**, and thus may lead at lower temperatures to a crystal phase slightly different from the gold analogue **1**. The electrical conductivity behavior of the gold compound $(DT–TTF)_4[Au(bdt)_2]_3$ (**2**), isostructural with **1**, showed again the second-order transition but at lower temperatures (183 K), which is related with the replacement of Se by S atoms in the complex ligand. We assume that the description for the structural transition occurring in compound **1** in the high temperature range is valid for **2**. The absence in **2** of the hysteretic transition at lower temperatures may be caused by a lower transition temperature (than for **1**) that makes this sluggish first-order transition too slow to be observed.

All these data reflect a relationship between crystal phases among the different systems of this family of compounds, in the sense that each system may switch to the same (or similar) structure but at different temperature range. This general situation is summarized in the diagram depicted in Fig. 14. Structure type A corresponds to the structure of **1** and **2** at room temperature, where the charge distribution among dimers is observed uniform due to a fast hopping regime. Structure type B presents a charge ordering and reduced electrical conductivity, with doubling of one (B1 in **2**) or two lattice parameters (B2 in **1**). Most likely, the B2 structure type corresponds to the packing pattern of **3** and **4** at high temperatures. Structure type C involves an additional lattice doubling in **1** and an incommensurate modulation in **3**. Their structural arrangement is not known yet. In spite of small individual differences between the structures of the different compounds, a general trend of phase transitions is clearly observed in this family of multiphasic DT_4M_3 compounds. These transition are quite sensitive to any chemical and/or crystal packing variations, induced by the metal or chalcogen substitution.

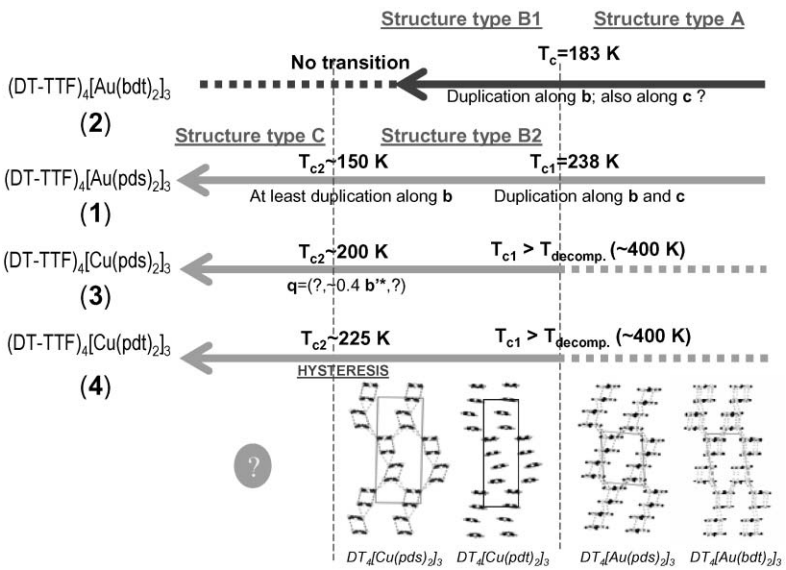

Fig. 14 Diagram summarizing all the phase transitions observed among the $(DT–TTF)_4[M(L)_2]_3$ family of compounds.

Concluding remarks

The compounds with general formula $(DT–TTF)_4[M(L)_2]_3$ (M = Au, Cu; L = pds, pdt, bdt) present at least three types of related structures with an identical packing pattern of donor and acceptor units. In these structures, the donors are strongly dimerized and interconnected through short S···S or Se···Se contacts in a bidimensional network. These compounds present multistability with a series of first- or second-order phase transitions. The structure and transition details are extremely sensitive to variations in the chemical structure as reflected by the metal or chalcogen substitution. Although a more clear analysis of these transitions has to wait for the detailed crystal structure determination of the different compounds, above and below their different transitions, so far precluded by crystal quality degradation, the results strongly suggest a common pattern of phase transitions between closely related structures. Finally, regarding possible applications of these materials as thermal sensor or switching devices, compounds **1** and **4** emerge as the most versatile systems due to the sharp hysteretic loop (each hysteresis of about 60 K wide range) observed in the magnetic properties, covering indeed a large temperature range (120–260 K).

Experimental

The synthesis of thieno[2,3-*d*]-1,3-dithiol-2-thione (DT–TTF) was performed as previously described.[15] The $(n\text{-}Bu_4N)[Au(pds)_2]$,[3] $(n\text{-}Bu_4N)[Cu(L)_2]$ (L = pds, pdt),[7] and $(n\text{-}Bu_4N)[Au(bdt)_2]$[9] salts were also prepared and purified by recrystallization as previously described.

FT-IR spectra were recorded on a Nicolet 710 spectrophotometer on KBr disks. UV–vis–NIR absorption spectra were obtained on a Varian Cary 5 spectrophotometer.

X-Ray data of $(DT–TTF)_4(Au(pds)_2)_3$ (**1**) has already been reported. X-Ray data for single crystals of $(DT–TTF)_4(Cu(pds)_2)_3$ (**3**), $(DT–TTF)_4(Cu(pdt)_2)_3$ (**4**) and $DT–TTF(Cu(pdt)_2)$ (**5**) were collected on a Nonius Kappa CCD diffractometer with monochromatic Mo Kα (λ = 0.71073 Å) radiation. Data were collected *via* ϕ and ω multiscans and reduced with the program DENZO-SMN without absorption correction. Measured reflections were corrected with the program SCALEPACK. The structures were refined by a full-matrix least-squares method using SHELXL97.[16] Least-squares calculation minimized $\Sigma w(\Delta F)^2$, being $w = [\sigma^2(F_o^2) + (aP)^2 + bP]^{-1}$, $P = (F_o^2 + 2F_c^2)/3$. Crystal parameters, data collection details and results of the refinements are summarized in Table 1. Crystal data for $(DT–TTF)_4(Au(bdt)_2)_3$ (**2**) were collected on a STOE diffractometer with image plate detector with monochromatic Mo Kα radiation (λ = 0.71073 Å) at 200 and 130 K. The structure was solved by direct methods using SIR97[17] programs and refined by a full matrix least squares method using SHELXL97 program.[16] Crystallographic data (excluding structure factors) for the structures reported in this paper have been deposited with the Cambridge Crystallographic Data Centre, CCDC reference numbers 259175 (**3**), 259176 (**4**) and 259177 (**5**). See http://dx.doi.org/10.1039/b505724h for crystallographic data in CIF format.

Electrical conductivity and thermoelectric power measurements were performed in the range 60–400 K in the same single crystal of each compound. In a first step thermopower was measured using a slow AC ($\sim 10^{-2}$ Hz) technique by attaching to the extremities of the needle shaped crystals with platinum paint (Demetron 308A), two ϕ = 25 μm 99.99% pure Au wires (Goodfellow Metals) anchored to two quartz thermal reservoirs, in a previously described apparatus,[18] controlled by a computer.[19] The oscillating thermal gradient was kept below 1 K, and it was measured with a differential Au-0.05 at.% Fe *versus* chromel thermocouple. The sample temperature was measured by a previously calibrated thermocouple of the same type. Both the differential thermocouple and the sample voltage were measured with Keithley 181 nanovoltmeters. The absolute thermopower of the sample was obtained after correction for the absolute thermopower of the Au leads, using the data of Huebner.[20] In a second step, electrical resistivity measurements were performed in the same sample using a four-probe technique. Without removing the crystal from the sample holder, two extra Au wires were placed on the sample in order to achieve a four-in-line contact configuration. Prior to the measurements the sample was checked for unnested to nested voltage ratio, as defined by Schaeffer *et al.*,[21] that was below 5%. Measurements were done imposing through the sample a current of 1 μA at low frequency (77 Hz) and measuring the voltage drop with a lock-in amplifier.

Magnetic susceptibility measurements in the range 4–300 K were performed using a longitudinal Faraday system (Oxford Instruments) with a 7 T superconducting magnet, under a magnetic field of 5 T and forward and reverse field gradients of 1 T m^{-1}. Polycrystalline samples (5–15 mg) were placed inside a previously calibrated thin wall Teflon bucket. The force was measured with a microbalance (Sartorius S3D-V). Under these conditions the magnetization was found to be proportional to the applied magnetic field.

EPR Spectra in the range 4–300 K were obtained with an X-Band Bruker ESP 300E spectrometer equipped with a rectangular cavity operating in T102 mode, a Bruker variable temperature unit and an Oxford EPR-900 cryostat, a Field Frequency lock ER 033M system and a NMR Gaussmeter ER 035M. The modulation amplitude was kept well below the line width and the microwave power was well below saturation.

The tight-binding band structure calculations were based upon the effective one-electron Hamiltonian of the extended Hückel method.[22] The off-diagonal matrix elements of the Hamiltonian were calculated according to the modified Wolfsberg–Helmholz formula.[23] All valence electrons were explicitly taken into account in the calculations, and the basis set consisted of single-ζ Slater-type orbitals. The exponents and ionization potentials used were taken from previous work.[2a,b]

Synthesis of $(DT–TTF)_4[Au(bdt)_2]_3$ (2)

Crystals of **2** were obtained by electrocrystallization with Pt electrodes. A solution of 9.0 mg of DT–TTF in 7.5 mL of CH_2Cl_2 was placed in the anode compartment. Immediately after an electrolyte solution of 10.2 mg of $(n\text{-}Bu_4N)[Au(bdt)_2]$

in 7.5 mL of CH_2Cl_2 previously prepared was placed in the cathode compartment. The system was sealed under argon, and a constant current of 0.5 μA was applied. After one week dark green needle-shaped crystals were obtained. The molar relation of the species was DT–TTF/Au(bdt)$_2$ = 1.00/0.5. IR (KBr pellet): $\tilde{\nu}$ (cm^{-1}) = 3097, 2924, 2855, 1470, 1345, 1320, 1260, 1104, 843, 754, 686.

Synthesis of (DT–TTF)$_4$[Cu(pds)$_2$]$_3$ (3)

Crystals of salt **3** were obtained by electrocrystallization with Pt electrodes from dichloromethane–acetonitrile 5 : 1 mixture, of the DT–TTF donor and the tetrabutylammonium salt of $[Cu(pds)_2]^-$ as electrolyte. An electrolyte solution of 3.206 mg of (n-Bu$_4$N)[Cu(pds)$_2$] in 10 mL of CH_3CN was prepared. An aliquot of 4 mL of the latter solution were added to a solution prepared with 3.208 mg of DT–TTF dissolved in 2 mL of CH_2Cl_2, and was placed in the anode compartment. The other 6 mL of electrolyte solution were immediately placed in the cathode compartment. The system was sealed under argon, and a constant current intensity of 1.5 μA was applied for three days. Dark black–green plate-shaped crystals grown on the anode correspond to the target compound (DT–TTF)$_4$[Cu(pds)$_2$]$_3$. The molar relation of the species was DT–TTF/Cu(pds)$_2$ = 1.00/0.37. IR (KBr pellet): $\tilde{\nu}$ (cm^{-1}) = 3095, 2919, 2851, 1467, 1409, 1346, 1315, 1258, 1131, 1101, 1026, 836, 800, 757.

Synthesis of (DT–TTF)$_4$[Cu(pdt)$_2$]$_3$ (4)

Crystals of salt **4** were obtained by electrocrystallization from dichloromethane–acetonitrile 5 : 1 mixture, of the DT–TTF donor and the tetrabutylammonium salt of $[Cu(pdt)_2]^-$ as electrolyte. An electrolyte solution of 1.642 mg of (n-Bu$_4$N)[Cu(pdt)$_2$] in 10 mL of CH_3CN was prepared. An aliquot of 4 mL of the latter solution were added to a solution prepared with 2.004 mg of DT–TTF dissolved in 2 mL of CH_2Cl_2, and was placed in the anode compartment. The other 6 mL of electrolyte solution were immediately placed in the cathode compartment. The system was sealed under argon, and a constant current intensity of 0.3 μA was applied for six days. Dark black–green plate-shaped crystals grown on the anode correspond to the target compound (DT–TTF)$_4$[Cu(pdt)$_2$]$_3$. The molar relation of the species was DT–TTF/Cu(pds)$_2$ = 1.00/0.43. However, the synthesis of **4** was not always reproducible, and under the same experimental conditions, another crystal phase of compound **5** was obtained as a contaminant (see below). IR (KBr pellet): $\tilde{\nu}$ (cm^{-1}) = 3079, 2919, 2850, 1470, 1414, 1376, 1349, 1322, 1298, 1194, 1142, 1104, 1060, 901, 848, 824, 753,482, 459, 440.

Synthesis of (DT–TTF)[Cu(pdt)$_2$] (5)

Under exactly the same concentrations of reactants and experimental conditions, compound **5** was obtained as dark pink shining plate-shaped crystals grown on the anode. The synthesis yielded randomly compound **5**, compound **4** or a mixture of them. IR (KBr pellet): $\tilde{\nu}$ (cm^{-1}) = 3057, 2925, 2850, 1470, 1415, 1345, 1325, 1301, 1199, 1147, 1106, 1064, 901, 847, 823, 800, 766, 707, 484, 459, 438.

Acknowledgements

This work was supported in Spain by DGI projects BQU2003-00760 and BFM2003-03372-C03, and by DGR Catalonia, projects 2001SGR00362 and 2001SGR333, and in Portugal by FCT under contract POCTI/35342/QUI/2000. The collaboration between authors in Barcelona and Sacavém was supported by the ICCTI-CSIC bilateral agreement, and additional support was provided through COST D14. JCD thanks EU for a Marie Curie fellowship during his stay at Orsay.

References

1 (*a*) E. Dagotto and T. M. Rice, *Science*, 1996, **271**, 618; (*b*) D. J. Scalapino, *Nature*, 1995, **377**, 12.

2 (*a*) C. Rovira, J. Veciana, E. Ribera, J. Tarres, E. Canadell, R. Rousseau, M. Mas, E. Molins, M. Almeida, R. T. Henriques, J. Morgado, J.-P. Schoeffel and J.-P. Pouget, *Angew. Chem., Int. Ed. Engl.*, 1997, **36**, 2324; (*b*) C. Rovira, *Chem.–Eur. J.*, 2000, **6**, 1723–1729; (*c*) E. Ribera, C. Rovira, J. Veciana, J. Tarrés, E. Canadell, R. Rousseau, E. Molins, M. Mas, J.-P. Schoeffel, J.-P. Pouget, J. Morgado, R. T. Henriques and M. Almeida, *Chem.–Eur. J.*, 1999, **5**, 2025–2039; (*d*) X. Ribas, M. Mas-Torrent, A. Pérez-Benítez, J. C. Dias, H. Alves, E. B. Lopes, R. T. Henriques, E. Molins, I. C. Santos, K. Wurst, P. Foury-Leylekian, M. Almeida, J. Veciana and C. Rovira, *Adv. Funct. Mater.*, 2005, **15**, 1023–1035.

3 J. C. Dias, J. Morgado, H. Alves, E. B. Lopes, I. C. Santos, M. T. Duarte, R. T. Henriques, M. Almeida, X. Ribas, C. Rovira and J. Veciana, *Polyhedron*, 2003, **22**, 2447–2452.

4 J. Morgado, M. T. Duarte, L. Alcácer, I. C. Santos, R. T. Henriques and M. Almeida, *Synth. Met.*, 1997, **86**, 2187–2188.

5 (*a*) W. Fujita and K. Awaga, *Science*, 1999, **286**, 261–262; (*b*) M. E. Itkis, X. Chi, A. W. Cordes and R. C. Haddon, *Science*, 2002, **296**, 1443–1445; (*c*) E. Laukhina, J. Vidal-Gancedo, V. Laukhin, J. Veciana, I. Chuev, V. Tkacheva, K. Wurst and C. Rovira, *J. Am. Chem. Soc.*, 2003, **125**, 3948–3953; (*d*) J. L. Brusso, O. P. Clements, R. C. Haddon, M. E. Itkis, A. A. Leitch, R. T. Oakley, R. W. Reed and J. F. Richardson, *J. Am. Chem. Soc.*, 2004, **126**, 8256–8265; (*e*) J. L. Brusso, O. P. Clements, R. C. Haddon, M. E. Itkis, A. A. Leitch, R. T. Oakley, R. W. Reed and J. F. Richardson, *J. Am. Chem. Soc.*, 2004, **126**, 14692–14693.

6 (*a*) H. Seo and H. Fukuyama, *J. Phys. Soc. Jpn.*, 1997, **6**, 1249; (*b*) H. Seo and H. Fukuyama, *Synth. Met.*, 2003, **135-136**, 673–675; (*c*) F. Y. Nad, P. Monceau and J. M. Fabre, *Phys. Rev. B*, 2000, **62**, 1753; (*d*) F. Y. Nad, P. Monceau and J. M. Fabre, *J. Phys. Condens. Matter*, 2000, **12**, L435; (*e*) P. Monceau, F. Y. Nad and S. Brasovskii, *Phys. Rev. Lett.*, 2001, **86**, 4080; (*f*) S. Aoyagi, K. Kato, A. Ota, H. Yamochi, G. Saito, H. Suematsu, M. Sakata and M. Takata, *Angew. Chem., Int. Ed.*, 2004, **43**, 3670–3673.

7 (*a*) X. Ribas, J. C. Dias, J. Morgado, K. Wurst, M. Almeida, J. Veciana and C. Rovira, *CrystEngComm*, 2002, **4**, 564–567; (*b*) X. Ribas, J. Dias, J. Morgado, K. Wurst, E. Molins, E. Ruiz, M. Almeida, J. Veciana and C. Rovira, *Chem.–Eur. J.*, 2004, **10**, 1691–1704.

8 E. B. Lopes, J. C. Dias, J. P. Seiça, I. C. Santos, J. Morgado, R. T. Henriques, M. Almeida, X. Ribas, K. Wurst, J. Veciana, C. Rovira and P. Foury-Leylekian, *J. Phys. IV*, 2004, **114**, 537–539.

9 M. J. Baker-Hawkes, E. Billig and H. B. Gray, *J. Am. Chem. Soc.*, 1966, **88**, 4870.

10 Since the mean planes of each DT–TTF units are not parallel (the angle between the mean plane of DT1 and DT2 is 2.17°, between DT2 and DT3 is 1.13°, and between DT3 and DT4 is 3.63°), the interplanar distance value over the molecules location is approximate.

11 Another way of defining the position of the anion units is the angle between the mean plane of the anion and the c-axis, which is 19.3° for CuSeComplex1 [20.9° for CuSComplex1] and 25.8° for CuSeComplex2 [25.3° for CuSComplex2].

12 (*a*) G. Beni, J. F. Kwak and P. M. Chaikin, *Solid State Commun.*, 1975, **17**, 1549; (*b*) P. M. Chaikin and G. Beni, *Phys. Rev. B*, 1976, **13**, 652.

13 (*a*) M.-H. Whangbo, J. M. Williams, P. C. W. Leung, M. A. Beno, T. J. Emge and H. H. Wang, *Inorg. Chem.*, 1985, **24**, 3500; (*b*) Since overlap is explicitly included in extended Hückel calculations, these interaction energies (β) should not be confused with the conventional transfer integrals (t). Although the two quantities are obviously related and have the same physical meaning, the absolute values of β are somewhat larger than those of t.
14 Selected bond distances within the Au and Cu complexes of compounds **1**, **3** and **4**, supporting their monoanionic character, can be found in the ESI†.
15 C. Rovira, J. Veciana, N. Santaló, J. Tarrés, J. Cirujeda, E. Molins, J. Llorca and E. Espinosa, *J. Org. Chem.*, 1994, **59**, 3307.
16 G. M. Sheldrick, University of Götingen: Götingen, 1997. SHELX97 – Programs for Crystal Structure Analysis (Release 97-2). G. M. Sheldrick, Institüt für Anorganische Chemie der Universität, Tammanstrasse 4, D-3400 Göttingen, Germany, 1998.
17 SIR97, A. Altomare, M. C. Burla, M. Camalli, G. L. Cascarano, C. Giacovazzo, A. Guagliardi, A. G. G. Moliterni, G. Polidori and R. Spagna, *J. Appl. Cryst.*, 1999, **32**, 115–119.
18 M. Almeida, S. Oostra and L. Alcácer, *Phys. Rev. B*, 1984, **30**, 2839.
19 E. B. Lopes, INETI- Sacavém, internal report, 1991.
20 R. P. Huebner, *Phys. Rev. A*, 1964, **135**, 1281.
21 P. E. Schaffer, F. Wudl, G. A. Thomas, J. P. Ferraris and D. O. Cowan, *Solid State Commun.*, 1974, **14**, 347.
22 M.-H. Whangbo and R. Hoffmann, *J. Am. Chem. Soc.*, 1978, **100**, 6093.
23 J. H. Ammeter, H.-B. Bürgi, J. Thibeault and R. Hoffmann, *J. Am. Chem. Soc.*, 1978, **100**, 3686.